

## Experimental determination of Sn $L$ -shell atomic parameters

F. Fernandez <sup>1</sup>, A. Sepúlveda <sup>2</sup>, S. Limandri,<sup>1</sup> J. Trincavelli,<sup>1</sup> and G. Castellano <sup>1,\*</sup>

<sup>1</sup>Universidad Nacional de Córdoba, Facultad de Matemática, Astronomía, Física y Computación; and Instituto de Física Enrique Gaviola (IFEG), CONICET–Medina Allende s/n, Ciudad Universitaria (5000) Córdoba, Argentina

<sup>2</sup>Facultad de Ciencias Naturales, Matemática y del Medio Ambiente, Universidad Tecnológica Metropolitana, 7800002 Santiago, Chile



(Received 22 June 2023; accepted 14 November 2023; published 30 November 2023)

A careful inspection on the tin  $L$  x-ray spectrum induced by electron impact was carried out, with the aim of obtaining fundamental atomic properties related to core ionizations and subsequent emissions. A bulk tin standard was irradiated, the resulting spectrum being recorded with a commercial wavelength dispersive spectrometer, and processed by means of a parameter optimization method previously developed. Characteristic energies, relative transition probabilities and natural linewidths were therefore experimentally determined for this element, and compared with data from the literature, when available. Satellite and radiative Auger effect structures were also investigated, for which the corresponding energy shifts and relative intensities were obtained. A number of these parameters were determined, even in overlapping peaks and weak transitions, which evidences the robustness of the spectral processing method used.

DOI: [10.1103/PhysRevA.108.052826](https://doi.org/10.1103/PhysRevA.108.052826)

### I. INTRODUCTION

The survey of atomic electron configurations through the intensity distribution for diagram and nondiagram emissions is useful to extract fundamental properties involved in atomic physics; this is helpful, for instance, to validate approaches that describe interaction among atomic electrons. A careful analysis of an x-ray emission spectrum allows to check if some particular assumptions apply to the possible single or multiple core-shell ionizations and the subsequent emission of radiation [1–3]. Experimental information can be extracted to account for the basic processes governing the interaction of radiation with matter by means of an appropriate description of the x-ray emission spectrum structure.

The different relaxation mechanisms following inner-shell ionizations can be described through a variety of fundamental magnitudes and phenomena: characteristic energies, radiative probabilities, satellite lines, radiative Auger emissions, and natural linewidths. All these magnitudes are of interest in many spectroscopic techniques which rely on the detection of the x rays emitted since, for instance, peak overlaps involving different lines may become an important inconvenience for the analyst.

Even when most  $K$  decays have been repeatedly studied, several transitions involving more external atomic shells remain incompletely investigated. The particular case of the tin  $L$  x-ray spectrum has scarcely been explored, although many applications increasingly involve the proper characterization of mixtures including this element, often by x-ray spectrometric techniques. An example is the popularity that indium-tin-oxide thin films [4] have gained as anode materials in organic electroluminescent display devices [5]. Recent

work explored a variety of uses, such as the peculiar interaction of electronic and magnetic properties in ceramics series of stannates solid solutions  $\text{BaFe}_x\text{Sn}_{1-x}\text{O}_{3-\delta}$  [6], the performance of Sn/Si/graphite composites for lithium-ion batteries storage [7], or the specific optical and electronic properties of SnSe nanoribbons obtained from two-dimensional (2D) layered materials [8].

In many of the mentioned studies, the fabrication of samples and devices involves characterization techniques based on x-ray emission, originated by inner-shell ionizations, where the fundamental parameters mentioned above become relevant. To experimentally obtain these parameters, the measured spectra must be processed by means of a reliable method, and all spectral contributions must be appropriately taken into account. In addition, these magnitudes bear basic information regarding the atomic electron configuration: for example, natural linewidths allow to correlate the intrinsic level widths of the states involved in each decay. For Sn- $L\alpha_1$  emission, this linewidth was measured on metallic samples by high-resolution x-ray fluorescence [9], and recently, the  $L\alpha_1$  and  $L\beta_{2,15}$  were studied by using a double-crystal vacuum spectrometer [10]. The scarce information available about natural linewidths was previously compiled by Campbell and Papp [11] for a large number of transitions, some additional measurements being performed by Ohno *et al.* [12]. Experimental characteristic energies were published by Bearden [13] and Cauchois and Sénémaud [14] for most elements, including tin; these latter authors also reported energies for satellite structures. Theoretical calculations for  $K$  and  $L$  decay energies were compiled by Deslattes *et al.* [2] for a wide range of atomic numbers. Radiative transition probabilities were predicted by Campbell and Wang [15] and Perkins *et al.* [16] for all elements and transitions, but experimental determinations are unusual, although they are crucial to validate the assumptions involved in the numerical assessments based

\*gcas@famaf.unc.edu.ar

on theoretical models, such as multiconfigurational Dirac-Hartree-Fock atomic-structure calculations [17]. Different approaches have been introduced in this kind of calculations to account for  $3d$   $K$  hypersatellite emissions [3,18,19], with uneven comparisons with experimental values [20]. Finally, some effort has been devoted to characterize the structures related with the radiative Auger effect (RAE) associated to  $K$  shells [21,22], a phenomenon which has recently drawn the attention for the case of isolated quantum structures [23,24]. However, experimental and theoretical data related to RAE bands corresponding to  $L$  shells are scarcely found in the literature.

The relevance underlying the knowledge of Sn satellite emissions is brought to evidence when analyzing the mixture In-Sn, since the Sn  $L_2M_1$  ( $L\eta$ ) diagram line (and its satellite) overlaps with the In- $L\alpha$  structure, the main  $L$  emissions, usually chosen in analytical techniques based on characteristic x-ray spectroscopy: the In- $L\alpha_2$  energy is 3.2793 keV and the In- $L\alpha_1$  energy is 3.2869 keV, whereas Sn- $L\eta$  lies at 3.2723 keV (7 eV below In- $L\alpha_2$ , always according to Ref. [13]). Although choosing the In- $L\beta$  lines appears as an interesting option, the  $L\beta_1$  energy is 3.4872 keV, very close to Sn- $L\alpha_1$  (at 3.4440 keV) and all surrounding satellite emissions (see below).

In this work, some of the mentioned relaxation parameters are obtained for tin through a detailed analysis of the  $L$  x-ray spectrum induced by electron impact. Fourteen diagram transitions to  $L$ -shell vacancy states arise from the experimental data acquired, characteristic energies being determined for them all, with the exception of the  $L\alpha_1$  emission (see below). In addition, relative radiative transition probabilities (RTPs) and natural linewidths were determined for all these decays, which also included the analysis of RAE bands and multiple ionization satellite structures. The complex deconvolutions involved were performed by a careful description of all the contributions revealed in the experimental spectrum through a robust fitting procedure implemented previously [25], which accounts for the refinement of atomic and instrumental parameters. It must be mentioned that, although the present work focuses on electron beam irradiation, the fundamental parameters determined apply to any ionization mechanism, with the obvious exclusion of the intensities of satellite and RAE emissions, tightly related to the nature and energy of the ionizing radiation used.

## II. EXPERIMENT

A pure bulk Sn standard was irradiated by a 16-keV electron beam in a JEOL JXA 8230 electron probe in which a Johansson-type wavelength dispersive spectrometer (WDS) is attached, the take-off angle being  $40^\circ$ . The x-ray  $L$  spectrum emitted was acquired by means of a PET analyzing crystal with an already characterized efficiency curve  $\varepsilon(E)$ , in terms of the detected photon energy  $E$  [26], and registered with a P10 flow counter. This curve was originally determined [27] from the comparison of two experimental spectra acquired from one single sample at the same incidence energy, one of them recorded with an energy dispersive spectrometer (EDS), and the second one with the WDS whose efficiency was surveyed. Regarding the uncertainties in the efficiency curve, it

must be mentioned that the solid angle subtended towards the EDS detector introduces the most important contribution, in this case being estimated as 5% [26]. The spectrometer energy resolution was estimated as  $(8.12 \pm 0.08)$  eV for the Sn- $\beta_1$  line at  $(3663.0 \pm 0.1)$  eV, after performing the optimization procedure described below.

The purity extent of the tin standard is high enough for the purposes pursued in the present work (99.998%); a careful survey was, however, carried out to check for eventual interferences from impurities, across a wavelength range sufficient to embrace all the emission energies analyzed. A beam current of  $(10.99 \pm 0.01)$  nA and an acquisition time of 2.5 s per spectrometer position were used to record a spectrum with 1017 bins. With these settings, a reasonable statistics was achieved, which enabled to adequately discriminate low intensity lines; for example, in the case of  $L\eta$ , one of the weakest lines, the relative statistical uncertainty remains below 3%. The behavior of the entire set of intensities recorded in the spectrum has been checked with other spectra acquired at similar incident beam energies, obtaining global fits as reasonable as the one achieved in the present work.

## III. SPECTRUM DESCRIPTION

The spectrum acquired was processed by using the software POEMA [25], in which atomic and experimental parameters can be optimized by a numerical procedure. This approach involves an analytical expression including tunable parameters that can be modified in a number of steps, until an optimal match with the set of measured intensities  $I_i$  recorded at channel  $i$  is achieved. The intensity  $\bar{I}_i$  is predicted as a function of the energy  $E_i$  for each of the  $N_c$  spectrum channels considered; the weighted sum of the quadratic differences between the experimental spectrum  $I_i$  and these estimated intensities is minimized through the optimization procedure by modifying the set of  $N_p$  parameters chosen in the assessment of  $\bar{I}_i$ . The parameters sought are therefore obtained through the numerical minimization of the estimator

$$\chi^2 = \frac{1}{N_c - N_p} \sum_{i=1}^{N_c} \frac{(\bar{I}_i - I_i)^2}{\bar{I}_i}.$$

After several optimization steps, the minimization procedure concludes, implying some convergence criterion in the determination of those atomic and instrumental parameters which have been allowed to vary. For each of the refined parameters, the expected dispersion is estimated by the propagation of the experimental uncertainties corresponding to the measured intensities  $I_i$ , a procedure carried out through numerical differentiation [28].

In the present case, attention was focused on the characteristic energies, RTPs, natural linewidths, and the energy and proportion of satellite lines and RAE bands. These parameters condition the assessment of the expression for the predicted intensities [29], which involves the bremsstrahlung spectrum leaving the sample, described according to the authors of Ref. [30], and the peak intensities  $P_q$ , modeled through the corresponding line shapes [31]. In the case of a diagram decay  $q$ , the number of x rays is estimated as

$$P_q = \beta \sigma_j^x p_q (ZAF)_q \varepsilon(E_q), \quad (1)$$

with  $\beta$  being proportional to the incident beam current;  $\sigma_j^x$  stands for the x-ray production cross section for the  $j$  subshell, i.e., the final vacancy production cross section  $\tilde{Q}_j$  times the fluorescence yield  $\omega_j$ ;  $p_q$  labels the radiative transition rate for this emission, and  $Z$ ,  $A$ , and  $F$  are the atomic number, absorption and fluorescence matrix correction factors, respectively. The absorption factor  $A$  can be considered uniform within the small wavelength interval involved in most of the peaks analyzed in this work; in some cases, however, the dependence of this factor on the photon energy must be taken into account carefully, even for only a linewidth interval [26].

It must be borne in mind that some spectral fits may often be artificially improved through an increase in the number of structures considered. However, along the present work the strategy followed always aimed to maintain the minimum number of peaks producing a reasonable fit. This means that, when a particular transition not previously reported was added, the appearance of this emission was evident in the experimental spectrum, which implied a noticeable fit worsening when this line was omitted.

The predicted peak intensities are not recorded as monoenergetic lines, but are spread in the emission process, and afterwards may be distorted by the detection system. A Voigt function  $S_q(E)$  was chosen here to model the characteristic peak profiles, representing a convolution of two probability distributions, a Gaussian  $G(E)$  which involves the instrumental features, and a Lorentzian  $L_q(E)$  whose width is representative of the mean lifetime of the initial vacancy state [32]

$$S_q(E) = \int L_q(E') G(E - E') dE'. \quad (2)$$

Complementary, Gaussian profiles were set to model the satellite lines, since this shape is more adequate to provide the joint effect corresponding to the numerous nondiagram transitions which give rise to each satellite structure. Instead, with the aim of taking into account the asymmetric shape of the RAE structures, the convolution of a Gaussian profile associated to detection effects and the profile suggested by Enkisch *et al.* [33] was implemented in the corresponding routine.

It is worth mentioning that the entire optimization process described above is not at all automatic. Several steps must be performed to achieve reliable results because of the complexity of the problem, inherent to approximately one hundred of variables involved: characteristic energies, RTPs, and natural linewidths for the 14 diagram lines and the 11 nondiagram structures in only one element like Sn, along with several global parameters such as subshell scale factors, detector response, energy calibration, and so on. The first of the mentioned steps involves delicate decisions about the number of transitions to be considered. A perfect fit can be achieved with a sufficiently large number of peaks, but this fit would completely lack of physical meaning. On the other hand, if some decay is omitted, the description would be poor and might turn out to be unphysical. The criterion always used is to assign the minimum number of transitions that properly describes the experimental spectrum, but this number is obtained after a long and artisanal process, plenty of advances, and setbacks.

## IV. RESULTS AND DISCUSSION

The measured and predicted Sn *L*-spectra are shown in Fig. 1, evidencing a very good agreement after the fitting process, which is reflected in the magnitude of the residues, also included in this graph. The 14 diagram lines identified and involved in the parameter refinement accomplished are labeled in this plot; for the sake of clarity, satellite lines and RAE structures have not been marked in the graph, although they are considered in the fitting procedure, as detailed above.

With the aim of achieving a set of reliable data through the refinement procedure, a cautious election for the successive steps must be followed, which should account for strong correlations among some parameters, particularly taking care of the adequate description of weak structures. The strategy pursued along the present work for the assessment of the parameters is similar to that used for the analysis of cadmium emissions, as described in Ref. [29]. For the present purposes, the product  $\beta \sigma_j^x$  in Eq. (1) constitutes a unique scaling factor for each subshell, which is refined as a single parameter in the optimization procedure.

### A. Characteristic energies

The entire fitting process starts with an energy calibration procedure [34] in which the emission energy of the most intense line ( $L\alpha_1$ ) is fixed according to the data reported by Bearden [13], i.e., 3.44398 keV. The energies for the diagram lines considered here obtained after the full refinement process are shown in Table I, along with the corresponding experimental data given by Bearden [13] and Cauchois and Sénémaud [14], and theoretical results by Deslattes *et al.* [2]. It is worth noticing that the spectral description achieved allows for energy uncertainties as low as 0.1 eV, much lesser than the instrumental resolution.

To better visualize the agreement of the values obtained here with those available in the literature, Fig. 2 shows the differences of the characteristic energies  $\Delta E$  obtained in this work with data reported by other authors. Since the data published by Bearden and Cauchois and Sénémaud are rather similar and share a common origin, this comparison only involves the first data set. The energies associated to the doublets reported in Ref. [2] were assessed through a weighted average which involves the relative transition probabilities given in Ref. [16].

It can be seen that these  $\Delta E$  values are lesser than 2 eV for 9 of the 13 transitions allowing this comparison. The energies obtained in the present work are indistinguishable from those reported in Ref. [2], always considering the uncertainties involved, excepting for the  $L_2N_4$  ( $\gamma_1$ ),  $L_2N_1$  ( $\gamma_5$ ),  $L_1M_5$  ( $\beta_9$ ), and  $L_1N_{2,3}$  ( $\gamma_{2,3}$ ) emissions. The transitions  $L\gamma_5$  and  $L\beta_9$  bear the weakest intensities in the corresponding *L* groups; in addition, both are located in the satellite region associated to the very intense  $L_3N_{4,5}$  ( $\beta_{2,15}$ ) doublet (see Fig. 1). The energy region surrounding the  $L_2N_4$  ( $\gamma_1$ ) line embraces four satellite emissions (see below), three of which have not been considered in previous compilations [14]; even disregarding all these emissions, the  $L\gamma_1$  characteristic energy cannot coincide with the values reported by these authors since the maximum intensity is located at most at 4.134 keV.

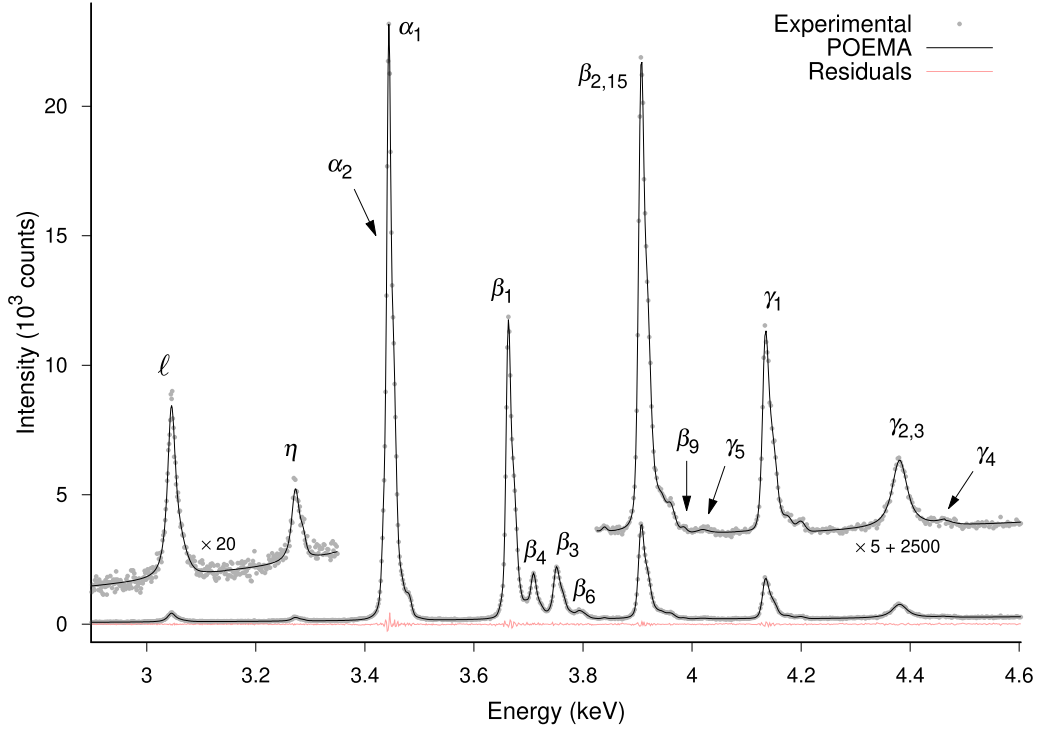


FIG. 1. Sn  $L$  spectrum measured at 16 keV. The insets show magnified views of the regions involving weak peaks.

It is worth noticing that, although the  $L_1N_{2,3}$  ( $\gamma_{2,3}$ ) emission energy is greater than the other values available for this comparison, the dispersion between those values is even larger than the  $\Delta E$  between the present result and the one given by Bearden, which suggests that this decay should be further investigated with special attention.

### B. Relative transition probabilities

Relative transition probabilities are the  $p_q$  parameters in Eq. (1) resulting from the optimization procedure and represent the probability for a particular radiative decay.

Given a vacancy produced in the  $L_i$  subshell, a series of radiative transitions can occur from different  $R_j$  outer shells; all these decays constitute the possible radiative transitions to the  $L_i$  vacancy and are therefore normalized to 100%. For the assessment of the RTP corresponding to the decay  $L_iR_j$ , the contribution of all satellite structures associated with this decay have been added to the main transition. The values obtained are shown in Table II, as well as the data reported by Campbell and Wang [15] and by Perkins *et al.* [16], which were normalized considering only the transitions identified along the present work. These latter databases result from theoretical assessments and interpolations, and do not involve

TABLE I. Characteristic energies (in keV) obtained for Sn. Numbers in parentheses indicate the estimated uncertainties in the last digits.

Transition	This work	Ref. [13]	Ref. [14]	Ref. [2]
$L_3M_1$ ( $\ell$ )	3.0452(3)	3.04499	3.04499	3.0447(14)
$L_3M_4$ ( $\alpha_2$ )	3.4351(2)	3.43542	3.43542	3.4360(10)
$L_3N_1$ ( $\beta_6$ )	3.791(1)	3.79260	3.7919	3.7929(36)
$L_3N_4$ ( $\beta_{15}$ )				3.90407(95)
$L_3N_5$ ( $\beta_2$ )	3.9066(1)	3.90486	3.9049	3.90532(95)
$L_2M_1$ ( $\eta$ )	3.2727(6)	3.27234	3.27234	3.2718(12)
$L_2M_4$ ( $\beta_1$ )	3.6630(1)	3.66280	3.6627	3.6631(11)
$L_2N_1$ ( $\gamma_5$ )	4.022(2)	4.0192	4.0190	4.0199(36)
$L_2N_4$ ( $\gamma_1$ )	4.1341(2)	4.13112	4.1311	4.1311(10)
$L_1M_2$ ( $\beta_4$ )	3.7090(2)	3.7083	3.7082	3.7081(21)
$L_1M_3$ ( $\beta_3$ )	3.7508(2)	3.7500	3.7503	3.7498(19)
$L_1M_5$ ( $\beta_9$ )	3.985(2)	3.9800	3.9798	3.9708(17)
$L_1N_2$ ( $\gamma_2$ )				4.3595(13)
$L_1N_3$ ( $\gamma_3$ )	4.3806(3)	4.3768	4.3769	4.3726(23)
$L_1O_{2,3}$ ( $\gamma_4$ )	4.465(4)	4.4638	4.4639	-

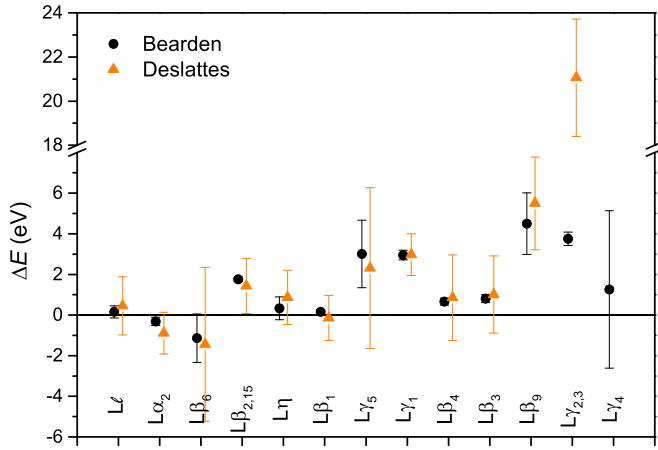


FIG. 2. Differences of the characteristic energies obtained in this work with data reported by other authors. The abscissas include the transitions in the same order as in Table I, except for  $L_3M_5$ , which is taken as reference. Circles: Ref. [13]; triangles: Ref. [2].

second-order or satellite transitions, which implies no rigorous comparison should be performed, but only as indicative of the thorough global trends.

The RTP values obtained here for the most intense lines are in good agreement with the values given in Refs. [15] and [16], discrepancies being around a few percents, or within the scatter between these other data. As expected, the largest relative differences occur for those transitions bearing very low emission probabilities.

### C. Natural linewidths

The function chosen for adequately representing the experimental diagram line profiles is a Voigt distribution [Eq. (2)], i.e., a convolution of the Lorentzian emission distribution whose full width at half maximum (FWHM) is the decay natural linewidth, with a Gaussian profile representing the instrumental broadening. This broadening is a function of the

TABLE II. Relative transition probabilities obtained for Sn. Numbers in parentheses indicate the estimated uncertainties in the last digits.

Transition	This work	Ref. [15]	Ref. [16]
$L_3M_1$ ( $\ell$ )	0.037(2)	0.03185	0.09100
$L_3M_4$ ( $\alpha_2$ )	0.061(2)	0.08639	0.08176
$L_3M_5$ ( $\alpha_1$ )	0.787(6)	0.76298	0.72495
$L_3N_1$ ( $\beta_6$ )	0.011(2)	0.00647	0.00677
$L_3N_{4,5}$ ( $\beta_{2,15}$ )	0.104(1)	0.11231	0.09552
$L_2M_1$ ( $\eta$ )	0.028(1)	0.02494	0.05375
$L_2M_4$ ( $\beta_1$ )	0.86(2)	0.85517	0.83852
$L_2N_1$ ( $\gamma_5$ )	0.0026(5)	0.00512	0.00651
$L_2N_4$ ( $\gamma_1$ )	0.111(3)	0.11476	0.10122
$L_1M_2$ ( $\beta_4$ )	0.333(8)	0.31337	0.31482
$L_1M_3$ ( $\beta_3$ )	0.48(1)	0.51080	0.51236
$L_1M_5$ ( $\beta_9$ )	0.008(1)	-	0.00594
$L_1N_{2,3}$ ( $\gamma_{2,3}$ )	0.172(3)	0.17050	0.16328
$L_1O_{2,3}$ ( $\gamma_4$ )	0.009(2)	0.00530	0.00360

TABLE III. Natural linewidths (in eV) for Sn obtained along this work. Numbers in parentheses indicate the estimated uncertainties in the last digits.

Transition	This work	Ref. [11]	Ref. [12]	Ref. [10]
$L_3M_1$ ( $\ell$ )	15(1)	12.03	12	
$L_3M_4$ ( $\alpha_2$ )	2.7(5)	2.86	-	
$L_3M_5$ ( $\alpha_1$ )	2.7(2)	2.87	-	3.34
$L_3N_1$ ( $\beta_6$ )	10(2)	5.83	6.3	
$L_3N_4$ ( $\beta_{15}$ )		2.59	3.2	2.72–4.13
$L_3N_5$ ( $\beta_2$ )	4(1)	2.51		
$L_2M_1$ ( $\eta$ )	14(2)	12.24	-	
$L_2M_4$ ( $\beta_1$ )	3.0(4)	3.07	-	
$L_2N_1$ ( $\gamma_5$ )	9(3)	6.04	-	
$L_2N_4$ ( $\gamma_1$ )	2.7(2)	2.72	-	
$L_1M_2$ ( $\beta_4$ )	5.9(5)	5.25	-	
$L_1M_3$ ( $\beta_3$ )	6.1(8)	5.7	-	
$L_1M_5$ ( $\beta_9$ )	9(3)	2.84	-	
$L_1N_2$ ( $\gamma_2$ )		19.4	20.3	
$L_1N_3$ ( $\gamma_3$ )	28(1)	19.4		
$L_1O_{2,3}$ ( $\gamma_4$ )	26(13)	-	-	

photon energy and is related to the interplanar spacing and the angular divergence  $\Delta\theta$  subtended by the analyzing crystal, as described in Refs. [27,32]. In the optimization procedure carried out, each peak profile is determined by two parameters refinable by POEMA: the corresponding natural linewidth and a unique  $\Delta\theta$  parameter for all lines present in the spectrum.

The values produced along this work for the natural linewidths are presented in Table III, which for comparison includes experimental data by Ohno *et al.* [12], as well as the values assessed by adding the widths of the energy levels participating in each decay, as published by Campbell and Papp [11]; the particular linewidths assessed in Ref. [10] for the  $L_3M_5$  and  $L_3N_4$  decays are also displayed in this table. It can be seen that the robustness of the approach chosen permitted to successfully deconvolve the profiles depicted above to obtain natural linewidths as low as, for example,  $(2.7 \pm 0.5)$  eV. A general agreement can be observed for most lines assessed, with the exception of  $L_3N_1$  ( $\beta_6$ ) and  $L_1M_5$  ( $\beta_9$ ). It is worth noticing that the energies for these two transitions have been reported with rather high uncertainties by the authors of Ref. [2]. In both cases, their very low intensities, along with the overlapping with different surrounding structures imply strong correlations between the parameters optimized, which hampers the assessment of the corresponding linewidths.

It should be emphasized that, despite the high uncertainty associated to the natural linewidth for the  $L_1O_{2,3}$  ( $\gamma_4$ ) transition reported here, it is possible to provide an estimate of the corresponding  $O_{2,3}$  level width, which results equal to  $(24 \pm 13)$  eV, considering the  $L_1$  width published in Ref. [11] (2.4 eV).

### D. Satellite lines

Several spectrum structures arise from second-order or spectator-hole transitions. The latter, for example, can distort the atomic energy levels to different extents, giving rise to out-of-diagram lines with energies slightly above the value

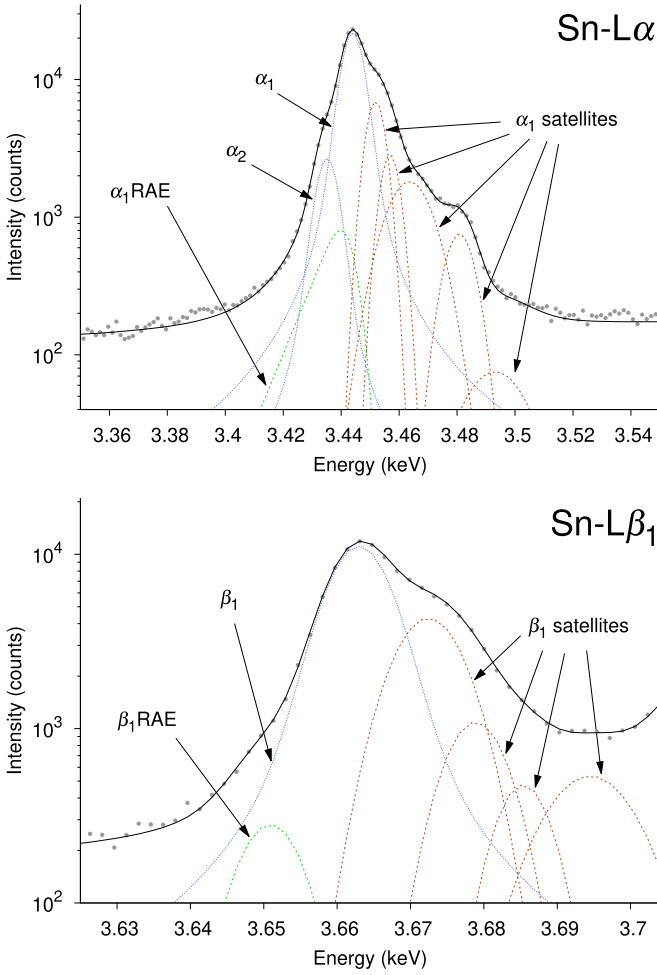


FIG. 3. Sn x-ray spectrum in the  $L\alpha$  and  $L\beta_1$  regions. Dots: experimental spectrum; solid line: spectral fitting; dashed line: contribution of each diagram, satellite, and RAE transition.

corresponding to the single hole emission associated. For example, in Ref. [10] some of the satellite emissions related to the  $L_3M_{4,5}$  ( $L\alpha$ ) structure are attributed to  $L_1L_3M_{4,5}$  Coster-Kronig transitions.

The spectral regions involving the main  $L\alpha$  and  $L\beta_1$  structures are respectively displayed in Fig. 3; the contributions of the diagram peaks, satellite lines, and RAE structures are correspondingly labeled, and the final fitting curve is also included in the graph. These many transitions may not always be observed separately because of the important overlaps occurring within the linewidths involved, and also due to the limited energy resolution of the spectrometer employed. It is useful to account for their collective effect by modeling them through a limited number of out-of-diagram lines, which may, in fact, originate in a combination of different phenomena. As detailed in Ref. [29], the joint effect representing these satellite structures can be properly described by Gaussian profiles.

Some of the out-of-diagram emissions displayed in Fig. 3 are not visually evident from the experimental spectrum, as is the case of the  $\alpha_1$ RAE band and certain  $\beta_1$  satellite decays. However, when any of these lines is omitted, a significative fit worsening is observed.

TABLE IV. Relative energies and areas obtained for Sn satellite lines. Numbers in parentheses indicate the estimated uncertainties in the last digits.

Parent line	$\Delta E_{\text{sat}}$ (eV)		Relative area (%)
	This work	Ref. [14]	
$L_3M_1$ ( $\ell$ )	11(2)	-	24(5)
$L_3M_{4,5}$ ( $\alpha$ )	7.9(4)	7.7	24(1)
	12.9(3)	12.3	10(1)
	19.5(4)	20.4	15.0(2)
	36.8(2)	29.7	3.9(1)
	48(2)	33.7	0.9(1)
$L_3N_1$ ( $\beta_6$ )	9(2)	-	70(20)
	48(2)	-	7(2)
$L_3N_{4,5}$ ( $\beta_{2,15}$ )	11.0(3)	7.7	35(1)
	21(2)	32.5	19(1)
	39(1)	36.8	8.0(5)
	54.3(6)	48.1	9.7(4)
$L_2M_1$ ( $\eta$ )	14(2)	-	10(3)
$L_2M_4$ ( $\beta_1$ )	10(1)	8.9	38(2)
	16(2)	-	9(2)
	22.4(9)	17.9	3.2(2)
	31.6(5)	27.6	5.9(2)
$L_2N_4$ ( $\gamma_1$ )	11.3(7)	-	62(20)
	22(5)	-	40(10)
	45(2)	36.8	5(2)
	66(1)	-	9(2)
$L_1M_2$ ( $\beta_4$ )	11.1(6)	-	26(2)
$L_1M_3$ ( $\beta_3$ )	10.7(4)	-	54(3)
	28.0(7)	-	6.2(8)

For the out-of-diagram lines determined in this work, the energy shifts  $\Delta E_{\text{sat}}$  and relative areas are listed in Table IV. These  $\Delta E_{\text{sat}}$  values are assessed as the differences between the energy of the out-of-diagram line and that of the associated principal transition. The  $\Delta E_{\text{sat}}$  data published by Cauchois and S enemaud [14] were also incorporated for comparison to Table IV. The relative areas displayed in this table are defined as the ratio between the satellite intensity and the one corresponding to the main transition.

A fairly good agreement is observed for the energies of the satellite structures determined here and the values given in Ref. [14]. Several out-of-diagram lines are obtained in the present work, as shown in this table: one new associated to each of the  $L_3M_1$ ,  $L_2M_1$ ,  $L_2M_4$ , and  $L_1M_2$  decays; two new lines for the  $L_3N_1$  and  $L_1M_3$  transitions; and three new attached to the  $L_2N_4$  diagram line. It is important to mention that the energies assigned to these structures are, to a certain extent, dependent on the type and number of functions used for the fitting; this means that comparisons should not be carried out in an exhaustive fashion.

It must be stressed that no previous data for electron bombardment on Sn are available in the literature regarding the satellite relative intensities of Table IV (only a few structures were surveyed in Ref. [10] for photon incidence). Since these

TABLE V. Relative energies and areas obtained for Sn RAE bands. Numbers in parentheses indicate the estimated uncertainties in the last digits.

Parent line	$\Delta E_{\text{RAE}}$ (eV)	Relative area (%)
$L_3M_5 (\alpha_1)$	- 4.3(5)	6.3(5)
$L_2M_4 (\beta_1)$	- 12.2(6)	2.4(1)
$L_1M_3 (\beta_3)$	- 12.0(7)	12(1)

intensities depend on projectile nature and also on its energy, care must be taken when performing comparisons.

### E. Radiative Auger emission

Individual vacancy states can also relax through radiative Auger emissions, resulting from the simultaneous release of an outer (Auger) electron with the emission of an x-ray photon [26]. In a RAE  $L_iR_jT_k$  transition following an ionization in the  $L_i$  shell, an electron from an external  $T_k$  orbital is ejected with a kinetic energy  $E_{\text{kin}}$  and an electron from the  $R_k$  decays to the  $L_i$  shell with the consequent emission of a photon whose energy  $E_{\text{RAE}}$  must satisfy the energy balance equation [27]

$$E_{\text{RAE}} = E(L_i) - E(R_j) - E(T_k) - E_{\text{kin}}, \quad (3)$$

$E(L_i)$ ,  $E(R_j)$ , and  $E(T_k)$  being the binding energies of the corresponding subshell. According to this expression, the photons associated with RAE effect constitute a band extending to a maximum energy given by Eq. (3) with  $E_{\text{kin}} = 0$  (the Auger electron is ejected with no kinetical energy). Experimentally, this band can be described by means of the convolution of the function given by Enkisch *et al.* [33] and a Gaussian function accounting for the instrumental broadening. The energy  $E_m$  corresponding to the maximum of this function is very close to the maximum energy of the RAE band, and the difference between this energy and the one corresponding to the parent line can be used to elucidate the shell from which the Auger electron was ejected.

The energy shifts  $\Delta E_{\text{RAE}} = E_m - [E(L_i) - E(R_j)]$  and relative areas for the RAE structures found in this work for the RAE bands are displayed in Table V. As in the case of the satellite lines, the relative areas are defined as the ratios of each band intensity to the main transition intensity. On the basis of the previous equation (3), specific information about the absorption edges involved in each RAE band may be inferred since the  $\Delta E_{\text{RAE}}$  shifts are close to the corresponding Auger electron binding energy, except for a change of sign. Comparing the  $\Delta E_{\text{RAE}}$  values obtained for  $L_2M_4 (\beta_1)$  and  $L_1M_3 (\beta_3)$  emissions with the of  $O_1$  binding energy given by Refs. [35] and [16] (between 12 and 13.4 eV), it can be concluded that these cases correspond to  $LMO_1$  RAE bands. In the case of the band connected to the  $L_3M_5 (L\alpha_1)$  emission, this assignment is not so simple since the lack of accurate information about the  $O_{2,3}$  levels hinders this identification. The data available in the literature suggest that these binding energies range from 5.77 eV [16] to 7.34 eV [35], which are slightly greater than the shift of 4.3 eV found here; it is difficult to conclude from which shell the Auger electron

is ejected, but the most likely identification appears to be an  $L_3M_5O_{2,3}$  RAE process.

## V. CONCLUSION

Characteristic energies, relative radiative transition probabilities, and natural linewidths were experimentally determined for 14 Sn *L* diagram decays induced by electron bombardment. The complete spectral analysis by means of a robust software package included several spectator hole satellite lines and RAE bands associated with some of the main lines.

The resulting data obtained for characteristic energies show a very good agreement with values published in the literature, deviations being in general lower than 2 eV when compared with the existing experimental database [13]. Since no experimental data for *L*-shell RTPs have been reported for tin, the set of values obtained along this work have been only compared with the theoretical calculations and interpolations available [15,16], exhibiting a good overall agreement.

A set of natural linewidths was determined for the diagram transitions studied here. Since no experimental dataset for all these linewidths can be found in the literature, the values obtained were compared, in most cases, with those resulting after adding the energy level widths of the states participating in each transition. A good general agreement has been observed, the values obtained here being slightly greater in most cases. Both the probabilities and natural widths for two diagram lines  $L_2N_1$  and  $L_3N_1$  exhibit the largest deviations from those existing in the literature; since their intensities are rather low, examining them with improved statistics and resolution is recommended. The  $L_1O_{2,3}$  linewidth was reported here, and using the  $L_1$  level width given by Ref. [16] allows to provide a rough estimate for the  $O_{2,3}$  level width, resulting in  $(23 \pm 14)$  eV.

Additionally, satellite decays associated to the presence of spectator holes and RAE structures were also studied. When possible, the energy of 14 satellites were compared with the experimental data from Ref. [14], obtaining a good agreement. Ten new satellite structures were detected, which were necessarily included in the fit to obtain a good spectrum description. The area of these satellite structures represent an important portion of the main emission, reaching the same order as the parent peak in some cases.

Three RAE structures were detected and associated with the most intense characteristic decays to each *L* subshell, the position of the maxima and the intensity of these structures, relative to the parent lines, being determined. The comparison of the relative energies permitted to infer that these are RAE transitions involving Auger electrons ejected from the *O* shells.

## ACKNOWLEDGMENTS

This work was financially supported by the Secretaría de Ciencia y Técnica (Universidad Nacional de Córdoba). The authors are also grateful to the Laboratorio de Microscopía Electrónica y Análisis por Rayos X (LAMARX) of the Universidad Nacional de Córdoba, Argentina, where the experimental determinations were performed.

- [1] J. H. Scofield, *Phys. Rev. A* **10**, 1507 (1974).
- [2] R. D. Deslattes, E. G. Kessler, Jr., P. Indelicato, L. de Billy, E. Lindroth, and J. Anton, *Rev. Mod. Phys.* **75**, 35 (2003).
- [3] R. Diamant, S. Huotari, K. Hämäläinen, R. Sharon, C. C. Kao, and M. Deutsch, *Phys. Rev. A* **79**, 062511 (2009).
- [4] V. Christou, M. Etchells, O. Renault, P. J. Dobson, O. V. Salata, G. Beamson, and R. G. Egdell, *J. Appl. Phys.* **88**, 5181 (2000).
- [5] H. Ishii, K. Sugiyama, E. Ito, and K. Seki, *Adv. Mater.* **11**, 605 (1999).
- [6] E. A. Bikyashev, A. V. Popov, S. P. Kubrin, P. Yanda, M. B. Mayorov, A. Trigub, V. A. Shuvaeva, A. Sundaresan, I. P. Raevski, and N. V. Ter-Oganessian, *Ceram. Int.* **48**, 7951 (2022).
- [7] A. Ruderman, S. Smrekar, M. V. Bracamonte, E. N. Primo, G. L. Luque, J. Thomas, E. Leiva, G. A. Monti, D. E. Barraco, and F. Vaca Chávez, *Phys. Chem. Chem. Phys.* **23**, 3281 (2021).
- [8] F. Davitt, K. Rahme, S. Raha, S. Garvey, M. R. Gutierrez, A. Singha, S. L. Y. Chang, S. Biswas, and J. D. Holmes, *Nanotechnology* **33**, 135601 (2022).
- [9] P. Putila, H. Juslén, M. Pessa, and G. Graeffe, *Phys. Scr.* **20**, 41 (1979).
- [10] S. Sakakura, H. Oohashi, Y. Ito, T. Tochio, A. M. Vlaicu, H. Yoshikawa, E. Ikenaga, and K. Kobayashi, *Radiat. Phys. Chem.* **75**, 1477 (2006).
- [11] J. L. Campbell and T. Papp, *At. Data Nucl. Data Tables* **77**, 1 (2001).
- [12] M. Ohno, P. Putila-Mantyla, and G. Graeffe, *J. Phys. B: At. Mol. Phys.* **17**, 1747 (1984).
- [13] J. A. Bearden, *Rev. Mod. Phys.* **39**, 78 (1967).
- [14] Y. Cauchois and C. SÉNÉMAUD, *Wavelengths of X-Ray Emission Lines and Absorption Edges* (Pergamon, New York, 1978).
- [15] J. L. Campbell and J.-X. Wang, *At. Data Nucl. Data Tables* **43**, 281 (1989).
- [16] S. T. Perkins, D. E. Cullen, M. H. Chen, J. H. Hubbell, J. Rathkopf, and J. H. Scofield, Tech. Rep. No. UCRL-50400 30 (Lawrence Livermore National Laboratory, Livermore, CA, 1991).
- [17] C. Froese Fischer, G. Gaigalas, P. Jönsson, and J. Bieroń, *Comput. Phys. Commun.* **237**, 184 (2019).
- [18] R. Diamant, S. Huotari, K. Hämäläinen, R. Sharon, C. C. Kao, and M. Deutsch, *Phys. Rev. Lett.* **91**, 193001 (2003).
- [19] K. Koziol and J. Rzadkiewicz, *At. Data Nucl. Data Tables* **131**, 101298 (2020).
- [20] J. Rzadkiewicz, D. Chmielewska, Z. Sujkowski, M. Berset, J.-C. Dousse, Y.-P. Maillard, O. Mauron, P.-A. Raboud, M. Polasik, K. Ślabkowska, J. Hoszowska, and M. Pajek, *Nucl. Instrum. Methods Phys. Res., Sect. B* **235**, 110 (2005).
- [21] H. R. Verma, *J. Phys. B: At. Mol. Opt. Phys.* **33**, 3407 (2000).
- [22] H. A. Melia, C. T. Chantler, L. F. Smale, and A. J. Illig, *J. Phys. B: At. Mol. Opt. Phys.* **53**, 195002 (2020).
- [23] M. C. Löbl, C. Spinnler, A. Javadi, L. Zhai, G. N. Nguyen, J. Ritzmann, L. Midolo, P. Lodahl, A. D. Wieck, A. Ludwig, and R. J. Warburton, *Nat. Nanotechnol.* **15**, 558 (2020).
- [24] C. Spinnler, L. Zhai, G. N. Nguyen, J. Ritzmann, A. D. Wieck, A. Ludwig, A. Javadi, D. E. Reiter, P. Machnikowski, R. J. Warburton, and M. C. Löbl, *Nat. Commun.* **12**, 6575 (2021).
- [25] R. Bonetto, G. Castellano, and J. Trincavelli, *X-Ray Spectrom.* **30**, 313 (2001).
- [26] A. Sepúlveda, T. Rodríguez, P. D. Pérez, A. P. L. Bertol, A. C. Carreras, J. Trincavelli, M. A. Z. Vasconcellos, R. Hinrichs, and G. Castellano, *J. Anal. At. Spectrom.* **32**, 385 (2017).
- [27] T. Rodríguez, A. Sepúlveda, A. Carreras, G. Castellano, and J. Trincavelli, *J. Anal. At. Spectrom.* **31**, 780 (2016).
- [28] R. D. Bonetto, A. C. Carreras, J. C. Trincavelli, and G. E. Castellano, *J. Phys. B: At. Mol. Phys.* **37**, 1477 (2004).
- [29] F. Fernandez, A. Sepúlveda, J. Trincavelli, and G. Castellano, *Ultramicroscopy* **232**, 113401 (2022).
- [30] J. Trincavelli and G. Castellano, *Spectrochim. Acta, Part B* **63**, 1 (2008).
- [31] S. P. Limandri, J. C. Trincavelli, R. D. Bonetto, and A. C. Carreras, *Phys. Rev. A* **78**, 022518 (2008).
- [32] S. P. Limandri, R. D. Bonetto, H. O. Di Rocco, and J. C. Trincavelli, *Spectrochim. Acta, Part B* **63**, 962 (2008).
- [33] H. Enkisch, C. Sternemann, M. Paulus, M. Volmer, and W. Schülke, *Phys. Rev. A* **70**, 022508 (2004).
- [34] P. D. Pérez, A. C. Carreras, and J. C. Trincavelli, *J. Phys. B: At. Mol. Opt. Phys.* **45**, 025004 (2012).
- [35] T. A. Carlson, in *Photoelectron and Auger Spectroscopy* (Springer, Boston, 1975), pp. 337–343.